


Tunable valley splitting in two-dimensional $\text{CrI}_3/\text{MSi}_2\text{P}_4$ ($M = \text{Mo}, \text{W}$) heterostructures: Interlayer coupling effects

Yunxi Qi, Can Yao, and Jun Zhao ^{*}

*New Energy Technology Engineering Laboratory of Jiangsu Province and School of Science,
Nanjing University of Posts and Telecommunications, Nanjing, Jiangsu 210023, China*

Hui Zeng [†]

School of Microelectronics, Nanjing University of Science and Technology, Nanjing, Jiangsu 210094, China



(Received 6 June 2023; accepted 29 August 2023; published 15 September 2023)

Valleytronics has become an emerging field for both theoretical and experimental research. Based on first-principles calculations, we demonstrate that the spin valley coupling and valley splitting properties of the $\text{Mo}/\text{WSi}_2\text{P}_4$ monolayers can be modulated by using the two-dimensional ferromagnetic CrI_3 semiconductor via the magnetic proximity effect. We show that the $\text{CrI}_3/\text{MoSi}_2\text{P}_4$ ($\text{CrI}_3/\text{WSi}_2\text{P}_4$) heterostructures are thermally stable and exhibit type-II band alignment at room temperature, leading to their possible applications for optoelectronic devices at ambient conditions. Moreover, we estimate the Curie temperature of the $\text{CrI}_3/\text{MoSi}_2\text{P}_4$ ($\text{CrI}_3/\text{WSi}_2\text{P}_4$) heterostructures and find that both valley splitting and valley-contrasting transport properties are expected to be enhanced below Curie temperature. Meanwhile, the valley polarization can be tuned by changing the magnetization direction and layer spacing. Most importantly, due to the influence of the Si-P sublayer, the valley-related properties of the $\text{CrI}_3/\text{MoSi}_2\text{P}_4$ ($\text{CrI}_3/\text{WSi}_2\text{P}_4$) heterostructures are predicted to be quite robust. The calculated Berry curvature and circular polarization indicate that the $\text{CrI}_3/\text{MoSi}_2\text{P}_4$ ($\text{CrI}_3/\text{WSi}_2\text{P}_4$) heterostructures can achieve the valley/spin Hall effect. Our research provides a comprehensive understanding of valley splitting in MA_2Z_4 -based heterostructures.

DOI: [10.1103/PhysRevB.108.125304](https://doi.org/10.1103/PhysRevB.108.125304)

I. INTRODUCTION

The valley is defined as the extreme value of the electron energy in the momentum space of a crystal [1]. Analogous to charge and spin, a valley is considered a new degree of freedom for electrons. The nonequilibrium distribution of electrons in these valleys can be used to implement information encoding [2,3]. In recent years, valleytronics in two-dimensional (2D) systems has received enormous attention, including single-layer transition metal dichalcogenides (TMDs) [4]. Owing to inversion symmetry breaking and spin-orbit coupling (SOC), spin-valley locking and opposite Berry curvatures in the K and K' valleys are theoretically predicated in single-layer TMDs. Furthermore, some valley-related physical phenomena, such as the valley Hall effect, spin Hall effect, and valley-resolved optical selection rule, have been experimentally observed [5–8]. Exploring novel 2D semiconductors and developing more 2D material platforms to achieve valley-related properties are crucial for potential applications of valleytronic devices [9].

Recently, Hong *et al.* prepared a new class of a 2D MA_2Z_4 ($M = \text{Mo}, \text{W}, \text{V}, \text{Nb}, \text{Ta}, \text{Ti}, \text{Zr}, \text{Hf}, \text{and Cr}; A = \text{Si and Ge}$;

$Z = \text{N, P, and As}$) monolayer [10]. Their excellent mechanical properties, high intrinsic photogenerated carrier mobility, and Poisson's ratio have promoted the study of layered MA_2Z_4 materials [10–12]. The high mobility and outstanding structural stability at ambient conditions for 2D MA_2Z_4 materials could allow practical applications in the future. For example, the intrinsic inversion symmetry breaking and strong SOC in MSi_2X_4 ($M = \text{Mo and W}; X = \text{N, P, and As}$) lead to not only valley-contrasting transport but also optical selection rules for spin and valley coupling [13,14]. Moreover, previous calculations demonstrated that the ferromagnetic substrate can be used to modulate valley splitting and valley polarization due to the magnetic proximity effect breaking the time reversal symmetry, resulting in Zeeman-type splitting and valley degeneracy in the $\text{MoSi}_2\text{N}_4/\text{CrCl}_3$ van der Waals (vdW) heterostructure [15]. The valley polarization can also be induced by applying an electric field to the ferroelectric valley material VSi_2P_4 [16].

Owing to the time reversal symmetry protection, most MA_2Z_4 monolayers cannot generate spontaneous valley polarization [17–19]. At present, several theoretical routes have been proposed to lift the degeneracy of the K and K' valleys to obtain the valley polarization properties. For example, the optical selection rule of different valleys is used to realize valley polarization [20]. However, due to the extreme difficulty in manipulating optical pumps, experimental measurements cannot always provide convincing and stable results. Another method to achieve valley polarization is applying a

^{*} Author to whom correspondence should be addressed. zhaojun@njupt.edu.cn

[†] Author to whom correspondence should be addressed. zenghui@njst.edu.cn

large Zeeman magnetic field [21]. However, a previous experimental observation showed that a 1 T magnetic field can generate only valley polarization of 0.1–0.3 meV. In addition to the above methods, magnetic atom doping [22] and magnetic proximity effect [23] are also promising methods for manipulating valley polarization in 2D materials. In particular, introducing the magnetic proximity effect by constructing vdW heterostructures is extremely intriguing because the formation of versatile vdW heterostructures gives rise to unlimited possibilities to manipulate the valleytronics properties by choosing different substrates [23]. More recent research showed that significant valley splitting in TMDs can be achieved by using ferromagnetic substrates, such as EuO [24] and CrI₃ [25,26]. In addition, lattice mismatch also could weaken valley splitting. The vertical vdW heterostructures constructed from layered materials can minimize the impact of lattice mismatch [27]. The ferromagnetic CrI₃ monolayer is a promising substrate candidate because the CrI₃ monolayer has both an out-of-plane magnetization axis and relatively clean interfaces to eliminate impurity scattering [28,29]. In this work, we choose the ferromagnetic CrI₃ monolayer to construct the Mo/WSi₂P₄ vdW heterostructures. The calculation results indicate that these two vdW heterostructures are thermally stable and have type-II band alignment at room temperature, allowing the possibility of their future use in solar cell devices. The Curie temperature of the CrI₃/MoSi₂P₄ (CrI₃/WSi₂P₄) heterostructures is estimated to be 48 (49) K. The CrI₃/MoSi₂P₄ and CrI₃/WSi₂P₄ heterostructures exhibit valley splitting and valley-contrasting transport properties when the work temperature is below the Curie temperature. Furthermore, our calculations reveal that both valley splitting and valley-contrasting transport properties could be prominently enhanced by using a vertical compressive strain. Our theoretical study enriches physical insight into the valleytronics in MA₂Z₄-based heterostructures.

II. COMPUTATIONAL METHODS

The structural optimization and the electronic property calculations are based on density functional theory in the Vienna Ab initio Simulation Package (VASP) [30,31], including the Mo/WSi₂P₄ monolayer, CrI₃ monolayer, and CrI₃/MSi₂P₄ ($M = \text{Mo}, \text{W}$) heterostructures. The projector augmented-wave pseudopotential is employed, and a cutoff energy of 500 eV is chosen [32]. The Perdew-Burke-Ernzerhof functional under the generalized gradient approximation is used to describe the exchange and correlation interaction [33]. The convergence criteria for total energy and atomic residual force are 1×10^{-8} eV and 0.001 eV/Å, respectively. The Brillouin zone is sampled by using an $8 \times 8 \times 1$ k -point grid for structural optimization and electronic structure calculation [34]. The vacuum layer along the Z-axis direction is set to 25 Å to avoid interactions introduced by the periodic boundary condition. In Table S1 in the Supplemental Material, we summarize the results of different van der Waals function corrections [35]. It can be seen that the interlayer distance D_0 calculated by using the optB86b-vdW and optB88-vdW [36] functionals is very close to that in a previous report [15]. Moreover, previous studies have shown that the optB86b-vdW functional provides excellent optimization of lattice parameters

and cleavage energy similar to experimental characterization when studying CrI₃ [37]. Therefore, the optB86b-vdW functional is adopted to deal with the vdW interactions [38]. Moreover, *ab initio* molecular dynamics (AIMD) simulations are performed at 300 K using a $2 \times 2 \times 1$ supercell to determine thermal stability. The VASPBERRY subroutine is used to calculate the Berry curvature and circularly polarized polarization of materials. All crystal structures are visualized through the VESTA software [39].

III. RESULTS AND DISCUSSION

Before constructing the CrI₃/MoSi₂P₄ and CrI₃/WSi₂P₄ heterostructures, we systematically studied the geometric and electronic structures of single-layer Mo/WSi₂P₄ and CrI₃ to ensure the reliability of subsequent results, as shown in Figs. S1 and S2. For MoSi₂P₄ and WSi₂P₄ monolayers, the valence band maximum (VBM) and conduction band minimum (CBM) are located at the high-symmetry K and K' points, exhibiting direct band gaps of 0.62 and 0.30 eV, respectively. Due to the inversion symmetry breaking in the single-layer structure, the spin splitting and Berry curvature contrasting features in the Dirac-type K and K' valleys are observed. The projected band structures shown in Figs. S2(a) and S2(b) indicate that the states near the band edges of the MoSi₂P₄ and WSi₂P₄ monolayers are mainly contributed by the d orbitals of the Mo atom. The s orbitals and p orbitals of P atoms also make small contributions to the VBM of the WSi₂P₄ monolayer. Figures S2(e) and S2(f) show that circularly polarized light can selectively activate carriers in desired valleys. The calculated band structure of single-layer CrI₃ is shown in Fig. S3. Figure S3(a) reveals distinct spin splitting for up- and down-spin components. When SOC is taken into account, there is a significant change in the top valence band of single-layer CrI₃, as shown in Fig. S3(b). Moreover, Fig. S3(c) shows the single-layer CrI₃ band structure calculated by the Hubbard U correction. Comparing Fig. S3(b) with Fig. S3(c), we find that the Hubbard U correction has no distinct impact on the electronic bands around the Fermi level. Furthermore, previous research [29] also indicated that the calculation of the CrI₃ monolayer does not need to consider the Hubbard U correction. Therefore, we ignore the Hubbard U correction for the calculation of vdW heterostructures. The electronic structure information for Mo/WSi₂P₄ and CrI₃ monolayers is summarized in Tables S2 and S3. All of the above results are consistent with previous studies [13,14,35,40].

In order to lift the degeneracy in the K and K' valleys, we construct CrI₃/MoSi₂P₄ and CrI₃/WSi₂P₄ heterostructures, as shown in Fig. 1. To diminish in-plane lattice mismatch, we use a 1×1 unit cell of monolayer CrI₃ and 2×2 unit cells of monolayer Mo/WSi₂P₄ to construct the CrI₃/MoSi₂P₄ (CrI₃/WSi₂P₄) vdW heterostructures. The mismatch of the heterostructures is estimated to be only 0.87% (0.76%). At present, it is difficult to accurately control the relative translation between different monolayers with experimental preparations. Therefore, in order to extrapolate a stable vdW stacking structure, three different stackings are considered. For the A₁ stacked CrI₃/MSi₂P₄ heterostructures, the Cr atom is located at the top of the M atoms ($M = \text{Mo}, \text{W}$). The A₂

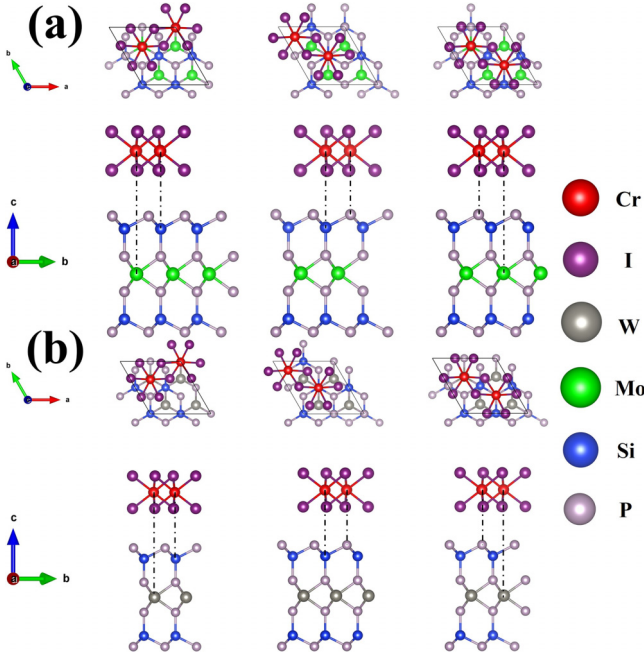


FIG. 1. Top view and side view of the optimized atomic structure of the $\text{CrI}_3/\text{MSi}_2\text{P}_4$ heterostructure, where (a) is the $\text{CrI}_3/\text{MoSi}_2\text{P}_4$ heterostructure and (b) is the $\text{CrI}_3/\text{WSi}_2\text{P}_4$ heterostructure, and the A_1 , A_2 , and A_3 stackings are shown from left to right. Red, deep purple, gray, green, blue, and lavender spheres represent Cr, I, W, Mo, Si, and P atoms, respectively.

stacking and A_3 stacking are obtained by in-plane translation of the CrI_3 monolayer along the diagonal line direction. Therefore, in the A_2 and A_3 stackings, Cr atoms are located at the top of Si and P atoms, respectively. The relevant structural information for $\text{CrI}_3/\text{MoSi}_2\text{P}_4$ and $\text{CrI}_3/\text{WSi}_2\text{P}_4$ heterostructures is summarized in Tables I and S4. Compared to differences from the A_1 stacking, only slight differences in in-plane lattice constants, interlayer spacing, and total energy occur between the A_2 and A_3 stackings. It is noticed that the calculated interlayer distance D_0 of different stacks is very close to the previously reported vdW heterostructures based on MA_2Z_4 [41,42]. The interlayer distance of different stacks is greater than the sum of the covalent radius of P and I atoms; the interface therefore is dominated by the vdW interaction. Because the A_2 and A_3 stacking structures of the $\text{CrI}_3/\text{MoSi}_2\text{P}_4$ and $\text{CrI}_3/\text{WSi}_2\text{P}_4$ heterostructures have a negligible influence on the electronic properties, experimental characterizations of the two stacked heterostructures are expected to be possible in future.

TABLE I. The lattice constants a and b for different stacked $\text{CrI}_3/\text{MoSi}_2\text{P}_4$ heterostructures, the shortest distance between Mo atoms and Cr atoms $d_{\text{Mo-Cr}}$, interlayer equilibrium distance D_0 , total energy E_t , and the band gap E_g without SOC.

$\text{CrI}_3/\text{MoSi}_2\text{P}_4$	$a = b$ (Å)	$d_{\text{Mo-Cr}}$ (Å)	D_0 (Å)	E_t (eV)	E_g (eV)
A_1	6.913	9.97	3.715	-193.9655	0.60
A_2	6.902	10.00	3.552	-194.0456	0.61
A_3	6.898	9.80	3.532	-194.0517	0.63

In order to determine the stability of this heterostructure, we further calculate the binding energy:

$$E_b = E_{\text{CrI}_3/\text{MSi}_2\text{P}_4} - E_{\text{CrI}_3} - E_{\text{MSi}_2\text{P}_4}, \quad (1)$$

where $E_{\text{CrI}_3/\text{MSi}_2\text{P}_4}$ is the total energy of the heterostructures and E_{CrI_3} and $E_{\text{MSi}_2\text{P}_4}$ are the total energies of the CrI_3 monolayer and MSi_2P_4 ($M = \text{Mo}, \text{W}$) monolayers, respectively. The E_b values of the A_2 and A_3 stacked $\text{CrI}_3/\text{MoSi}_2\text{P}_4$ ($\text{CrI}_3/\text{WSi}_2\text{P}_4$) heterostructures are -0.76 and -0.78 eV (-0.76 and -0.77 eV), respectively. The negative binding energy demonstrates that the formation of the heterostructures corresponds to an exothermic reaction. Due to the negligible differences in the calculated E_b values, three types of stackings are predicated to be achievable in experiments. In the Supplemental Material, we estimate the Curie temperature of the heterostructure. Compared with the original CrI_3 ($3.0\mu_B/\text{Cr}$) monolayer, the local magnetic moment of Cr in the $\text{CrI}_3/\text{MoSi}_2\text{P}_4$ ($\text{CrI}_3/\text{WSi}_2\text{P}_4$) heterostructures also increases by $0.19\mu_B$ ($0.20\mu_B$), where μ_B is the Bohr magneton. Therefore, the Heisenberg exchange constant increases to $J_0 = 2.73$ (2.81) meV, equivalent to a Curie temperature of 48 (49) K. The valley polarization operation of the $\text{CrI}_3/\text{MoSi}_2\text{P}_4$ and $\text{CrI}_3/\text{WSi}_2\text{P}_4$ heterostructures is expected to be achieved at a maximum temperature of 48 K. In addition, the heterostructures did not deform during AIMD simulation at 300 K, as shown in Fig. S4. Combined with the type-II band alignment of $\text{CrI}_3/\text{MoSi}_2\text{P}_4$ and $\text{CrI}_3/\text{WSi}_2\text{P}_4$ heterostructures, it is conducive to the preparation of $\text{CrI}_3/\text{MoSi}_2\text{P}_4$ and $\text{CrI}_3/\text{WSi}_2\text{P}_4$ heterostructures at room temperature and applications for solar cell devices. Taking the minimum total energy of the A_3 stacking into account, we thus explore the electronic structure properties and valley-related properties of this stacking hereafter.

The electronic structures, as well as the properties of valleytronics, of the $\text{CrI}_3/\text{MoSi}_2\text{P}_4$ and $\text{CrI}_3/\text{WSi}_2\text{P}_4$ heterostructures are similar. Therefore, we will discuss the former in detail. As presented in Fig. 2(a), the $\text{CrI}_3/\text{MoSi}_2\text{P}_4$ heterostructure has an indirect band gap, and the band gap is approximately 0.63 eV. According to the up spin component result, the VBM and the CBM are located at the K and G points, respectively. When SOC is excluded, the energy in the K and K' valleys is degenerate for the VBM. Regarding the conduction band, although the CBM is located at the G point, the conduction bands at the K and K' points form a local minimal energy value and also generate a pair of degenerate valleys at the CBM. The valley splitting is induced by the magnetic substrate. Figure 2(b) exhibits the atomic projected band structure with SOC. The band structure features of both the MoSi_2P_4 monolayer and CrI_3 monolayer are maintained. The valley splittings for the valence band Δ_{VB} and the conduction band Δ_{CB} are defined as

$$\Delta_{\text{VB}} = E_K^{\text{VB}} - E_{K'}^{\text{VB}}, \quad \Delta_{\text{CB}} = E_K^{\text{CB}} - E_{K'}^{\text{CB}}, \quad (2)$$

where E_K^{VB} and $E_{K'}^{\text{VB}}$ (E_K^{CB} and $E_{K'}^{\text{CB}}$) are the energy extreme values in the K and K' valleys in the valence band (conduction band). For the $\text{CrI}_3/\text{MoSi}_2\text{P}_4$ heterostructure, the conduction band valley splitting is 0.18 meV, and the valence band valley splitting is only -0.084 meV. For the valence band, the energy of the K' valley is higher than that of the K valley. To verify

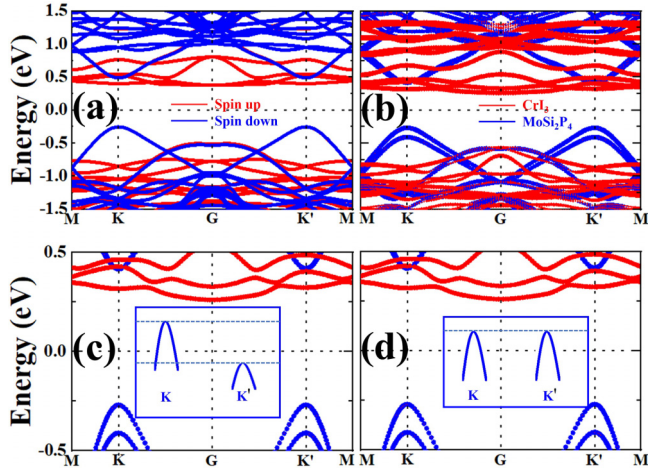


FIG. 2. (a) The band structure of the $\text{CrI}_3/\text{MoSi}_2\text{P}_4$ heterostructure without SOC, where the red (blue) lines represent the band structure of the spin-up (spin-down) component. (b)–(d) The band structures with SOC, where the red (blue) lines represent the band contributed by the CrI_3 (MoSi_2P_4) layer. In (b)–(d) the Cr magnetic moments are set along the $+z$, $-z$, and $+x$ directions, respectively. The insets in (c) and (d) represent the zoomed valence bands in the K and K' valleys.

the accuracy of weak valley splitting in the $\text{CrI}_3/\text{MoSi}_2\text{P}_4$ heterostructure, we have reversed the magnetization direction to examine the valley splitting, as shown in Fig. 2(c). We find that the energy of the K valley is higher than that of the K' valley after reversing the magnetization direction. Furthermore, Figs. 2(b) and 2(c) show that the band gap of the $\text{CrI}_3/\text{MoSi}_2\text{P}_4$ heterostructure containing the SOC effect is approximately 0.53 eV. The calculated results mentioned above indicate that the valley splitting is thought to be induced by the magnetic CrI_3 monolayer with the help of magnetization along $\pm z$ directions, although the splitting magnitude is tiny. Most importantly, Fig. 2(d) demonstrates that the valley splitting, in practice, cannot be generated by in-plane magnetization direction. Subsequently, our calculations will show that the valley splitting of the $\text{CrI}_3/\text{MoSi}_2\text{P}_4$ heterostructure can be significantly manipulated by applying vertical strain. The calculated electronic structure of the $\text{CrI}_3/\text{WSi}_2\text{P}_4$ heterostructure is shown in Fig. S5. It is found that the valley splitting of the $\text{CrI}_3/\text{WSi}_2\text{P}_4$ heterostructure is similar to that of the $\text{CrI}_3/\text{MoSi}_2\text{P}_4$ heterostructure. The total K and K' valley splitting is defined as $\Delta_{KK'} = \Delta_{\text{CB}} - \Delta_{\text{VB}}$. The total valley splitting of the $\text{CrI}_3/\text{WSi}_2\text{P}_4$ heterostructure is about 2.998 meV, which is equivalent to applying a magnetic field of about 15–30 T. Compared to the application of external magnetic field, introducing a ferromagnetic substrate is a more effective and convenient route to enhance the K and K' valley polarization of the MoSi_2P_4 monolayer [28].

To understand the physical mechanism of the enhancement of valley polarization, we calculate the charge density difference of the $\text{CrI}_3/\text{MSi}_2\text{P}_4$ heterostructures, as shown in Figs. 3(a) and S6(a). The charge density difference $\Delta\rho$ is defined as

$$\Delta\rho = \rho_{\text{CrI}_3/\text{MSi}_2\text{P}_4} - \rho_{\text{MSi}_2\text{P}_4} - \rho_{\text{CrI}_3} \quad (3)$$

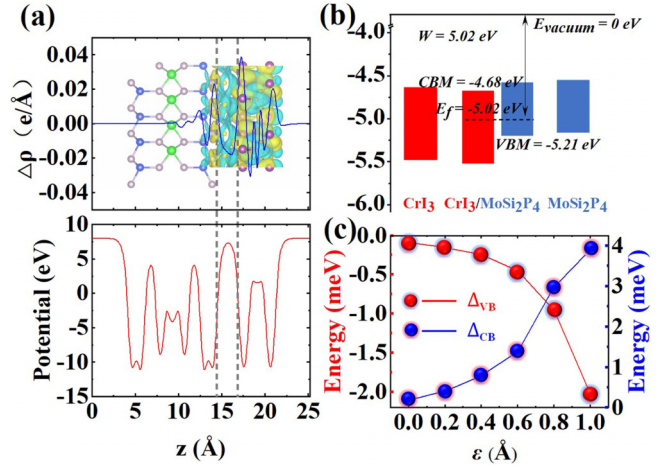


FIG. 3. (a) The top panel shows the plane average charge density difference of the $\text{CrI}_3/\text{MoSi}_2\text{P}_4$ heterostructure and the three-dimensional charge density difference of $0.0001 e/\text{bohr}^3$ iso-surface. The yellow and cyan surfaces represent the accumulation and depletion of charges in space, respectively. The plane-averaged charge density along the z direction $\rho(z)$ is defined as $\rho(z) = \int \Delta\rho(x, y, z) dx dy$. The bottom panel shows the planar average electrostatic potential of the $\text{CrI}_3/\text{MoSi}_2\text{P}_4$ heterostructure along the z direction, with a potential difference of 0.13 eV between the two monolayers. (b) The band alignment of the $\text{CrI}_3/\text{MoSi}_2\text{P}_4$ heterostructure. (c) The valley splitting of the $\text{CrI}_3/\text{MoSi}_2\text{P}_4$ heterostructure varied with respect to the interlayer distance. Δ_{VB} and Δ_{CB} represent valence band valley splitting and conduction band valley splitting, respectively.

where $\rho_{\text{CrI}_3/\text{MSi}_2\text{P}_4}$, $\rho_{\text{MSi}_2\text{P}_4}$, and ρ_{CrI_3} represent the charge density distributions of the $\text{CrI}_3/\text{MSi}_2\text{P}_4$ heterostructures, the MSi_2P_4 monolayers, and the CrI_3 monolayer, respectively. The planar-averaged charge density difference along the z axis of $\text{CrI}_3/\text{MSi}_2\text{P}_4$ heterostructures is included in Fig. 3. They all clearly indicate that substantial electron redistribution occurred at the contact interface. Specifically, the electron redistribution in the $\text{CrI}_3/\text{MSi}_2\text{P}_4$ heterostructure layer is mainly concentrated in external P and Cl atoms, indicating the existence of vdW attraction between the two monolayers. However, the average distance of $d_{\text{M-Cr}}$ is close to 10 Å, and excessive distance results in almost zero magnetic moment on M atoms; the exchange interaction is negligible. The data shown in Tables S4 and I are consistent with our analysis. In addition, the K and K' valleys in the $\text{CrI}_3/\text{MSi}_2\text{P}_4$ heterostructures are primarily contributed by M atoms, while M atoms induce almost negligible charge transfer. This is in contrast to previously studied heterostructures such as WSe_2/EuO [27] and $\text{WS}_2/h\text{-VN}$ [43]. The latter undergoes perceptible charge transfer at the W atom, and the substrate induces a finite magnetic moment in the WSe_2 monolayer. As a consequence, the charge transfer to the magnetic atom through large Coulomb interactions and exchange interactions is crucial for the manipulation of valley splitting. In addition, the electrostatic potential gradient also plays an important role in lifting valley degeneracy. Previous studies revealed that applying a vertical external electric field combined with a magnetic field can significantly increase the valley splitting of silicene [44,45], where the vertical electric field can be generated by interlayer

electrostatic potential gradients. The electrostatic potential in Figs. 3(a) and S6 indicates an almost zero potential difference between the CrI_3 monolayer and the MSi_2P_4 monolayer. Therefore, valley splitting in $\text{CrI}_3/\text{MSi}_2\text{P}_4$ heterostructures depends on time reversal symmetry violation, which is similar to the situation in $\text{CrI}_3/\text{WSe}_2$ heterostructures [46]. The band alignment can effectively reflect the electronic properties of heterostructures. By setting the vacuum energy level to zero, we can plot the band alignment of the CrI_3 monolayer, MSi_2P_4 monolayers, and $\text{CrI}_3/\text{MSi}_2\text{P}_4$ heterostructures, as shown in the Figs. 3(b) and S6(b). The VBM of $\text{CrI}_3/\text{MoSi}_2\text{P}_4$ ($\text{CrI}_3/\text{WSi}_2\text{P}_4$) heterostructures is contributed by the MoSi_2P_4 (WSi_2P_4) sublayer, while their CBM is contributed by the CrI_3 sublayer. Consequently, type-II band alignment is formed. It facilitates the separation of electron-hole pairs stimulated by light pumping, suggesting great potential applications of $\text{CrI}_3/\text{MSi}_2\text{P}_4$ heterostructures for solar cell devices.

Due to the fact that the electronic states in the K and K' valleys are mainly contributed by Mo atoms and Cr atoms are the main atoms providing local magnetic fields, Mo/W-Cr coupling is expected to play a key role in lifting valley degeneracy. By reducing the interlayer distance of heterostructures to enhance Mo/W-Cr coupling, valley splitting can be enhanced. Here, we define vertical strain as

$$\varepsilon = D_0 - D, \quad (4)$$

where D_0 is the equilibrium interlayer distance of the heterostructures and D is the interlayer distance after vertical strain is applied. ε corresponds to the magnitude of reduction in the interlayer spacing compared to the equilibrium case. The maximum value of $\varepsilon = 1 \text{ \AA}$ is equal to 28.31% of interlayer compressive strain, which can be achieved by controlling the interlayer spacing using external hydrostatic pressure [47]. The valley splitting changes in the calculated $\text{CrI}_3/\text{MoSi}_2\text{P}_4$ heterostructure are shown in Fig. 3(c). The valley splittings (Δ_{VB} and Δ_{CB}) of $\text{CrI}_3/\text{MoSi}_2\text{P}_4$ and $\text{CrI}_3/\text{WSi}_2\text{P}_4$ heterostructures increase with a decrease in interlayer distance. When $\varepsilon = 1 \text{ \AA}$, Δ_{VB} and Δ_{CB} of the $\text{CrI}_3/\text{MoSi}_2\text{P}_4$ heterostructure reach their maximum values (-2.03 and 3.91 meV). On the contrary, when $\varepsilon = 0.8 \text{ \AA}$, the maximum Δ_{CB} of the $\text{CrI}_3/\text{WSi}_2\text{P}_4$ heterostructure is -4.35 meV, as shown in Fig. S6(c). The calculation results indicate that interlayer strain can effectively tune K and K' valley splittings.

To explore the origin of valley splitting variations, we study the changes in magnetic moments affected by strain engineering. When $\varepsilon = 1 \text{ \AA}$, the distance between Mo atoms and Cr atoms is about 7.25 \AA , which is much greater than the previously reported vdW heterostructures of TMDs [48,49]. Therefore, we speculate that only small magnetic moments can be induced through ferromagnetic substrate coupling, as shown in Table S5. For the $\text{CrI}_3/\text{MoSi}_2\text{P}_4$ heterostructure, exchange interactions induce small magnetic moments close to $-0.003\mu_B$ in Mo atoms. As the strain increases, the magnetic moment of Mo atoms also increases linearly. When $\varepsilon = 1 \text{ \AA}$, the magnetic moment of Mo atom increases to its maximum value ($-0.025\mu_B$). Meanwhile, the outermost P atom is also significantly affected by the magnetic proximity effect. When $\varepsilon = 1 \text{ \AA}$, magnetic moments of $-0.059\mu_B$

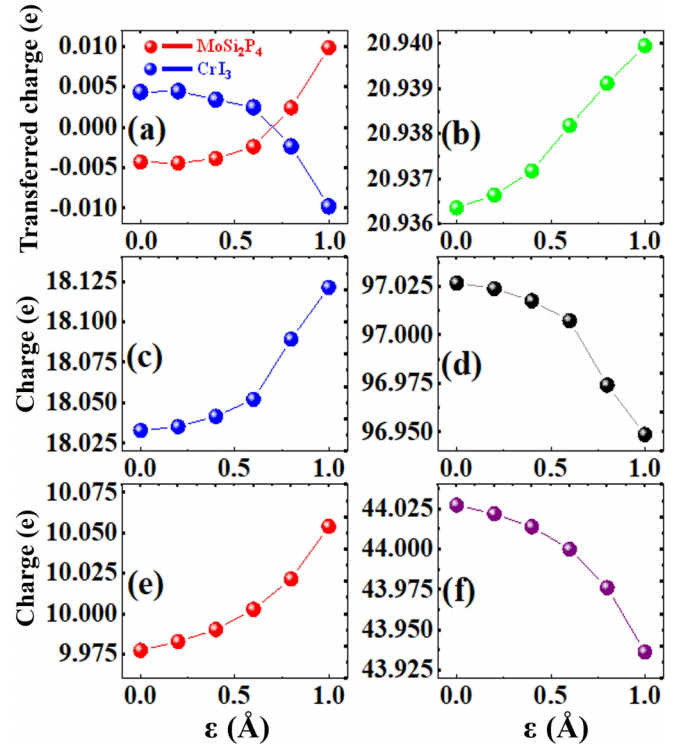


FIG. 4. The charge transfer of (a) the $\text{CrI}_3/\text{MoSi}_2\text{P}_4$ heterostructure based on the Bader charge analysis method varies with strain engineering. Positive and negative values indicate electron accumulation and depletion in the CrI_3 and MoSi_2P_4 monolayers, respectively. (b)–(f) are calculated using the Bader charge analysis method to calculate the variation of charge carriers with strain engineering. (b) is the sum of four Mo atoms, (c) is the sum of eight Si atoms, (d) is the sum of 16 P atoms, (e) is the sum of two Cr atoms, and (f) is the sum of six I atoms.

are induced through ferromagnetic substrate coupling, mainly contributed by P atoms near the CrI_3 monolayer. The magnetic moment variation of the $\text{CrI}_3/\text{WSi}_2\text{P}_4$ heterostructure is similar to that of the $\text{CrI}_3/\text{MoSi}_2\text{P}_4$ heterostructure. The increase in heterostructure Δ_{VB} and Δ_{CB} is mainly attributed to the induced magnetic moment of Mo and P atoms. In addition, carrier transfer is more sensitive to changes in interlayer distance. The CBM and VBM of the K and K' valleys are mainly contributed by Mo and P atoms. Therefore, based on Bader carrier analysis [50], we study the charge transfer of different monolayers and atoms, as shown in Figs. 4 and S7. Figures 4(a) and S7(a) confirm the substantial charge transfer between the MSi_2P_4 and CrI_3 monolayers, and the monotonic increase in Δ_{VB} and Δ_{CB} in the $\text{CrI}_3/\text{MoSi}_2\text{P}_4$ heterostructure is related to the electron accumulation of Mo atoms and the depletion of P atoms. However, the accumulation of Mo atomic charges shown in Fig. S7(b) first increases and then decreases with compressive strain. The comprehensive changes in charge transfer between Mo and P atoms lead to anomalous changes in Δ_{CB} of the $\text{CrI}_3/\text{WSi}_2\text{P}_4$ heterostructure.

Based on the above analysis, from the perspective of the magnetic proximity effect, the magnetic coupling aimed at conducting Mo/W atoms is actually shielded by the Si-P sublayer, resulting in robust valley-contrasting properties for

the MSi_2P_4 monolayer. This is in sharp contrast to conventional TMD-based heterostructures constructed by magnetic substrates. Therefore, we speculate that the electronic states and valley properties of MA_2Z_4 ($M = \text{Mo}, \text{W}, \text{Cr}; A = \text{Si}, \text{Ge}; Z = \text{N}, \text{P}, \text{As}$) heterostructures constructed with magnetic substrates are quite robust because the A - Z sublayer provides protection. Recent research also supports our inference [51,52]. The controllability and robustness of valley polarization in $\text{CrI}_3/\text{MSi}_2\text{P}_4$ heterostructures are expected to overcome the fluctuation of the valley signal. This is beneficial for the application of MA_2Z_4 -based heterostructures for valleytronics.

In addition, by applying an external electric field perpendicular to the plane, the interlayer charge distribution can be significantly changed, which is anticipated to enhance the valley splitting, as shown in Fig. S8. The calculated results show that with the application of an electric field of 0.001 V/\AA , the total valley splitting $\Delta_{KK'}$ of the $\text{CrI}_3/\text{MoSi}_2\text{P}_4$ heterostructure is increased to 0.36 meV , which is 36.4% higher than the original $\Delta_{KK'}$. Using a considerable vertical electric field is expected to increase the valley splitting value. At present, surface doping technology can induce strong surface electric fields on 2D materials. For example, when a strong vertical electric field of 0.72 V/\AA is applied, black phosphorus can transform into 2D semi-Dirac electron systems [53,54]. Recently, the use of the *in situ* potassium atom doping method instead of the traditional gate voltage enhancement successfully achieved this transformation, which may be beneficial for future applications of valleytronics [55,56]. Therefore, we suggest using similar methods to lift valley degeneracy. In addition, constructing a $\text{CrI}_3/\text{MSi}_2\text{P}_4/\text{CrI}_3$ trilayer and manipulating the layer alignment are expected to significantly lift valley degeneracy. This is fully demonstrated in the $\text{NiCl}_2/\text{WSe}_2/\text{NiCl}_2$ and $\text{CrI}_3/\text{WSe}_2/\text{CrI}_3$ heterostructures [46,57].

The valley-related transport properties are closely related to the Berry curvature $\Omega(k)$. For 2D systems, $\Omega(k)$ has only the z component, $\Omega_z(k)$, which can be calculated as follows:

$$\Omega_z(k) = - \sum_n \sum_{n' \neq n} f_n \frac{2 \text{Im} \langle \psi_{nk} | v_x | \psi_{n'k} \rangle \langle \psi_{n'k} | v_y | \psi_{nk} \rangle}{(E_n - E_{n'})^2}, \quad (5)$$

where v is the velocity operator, f_n is the equilibrium Fermi-Dirac distribution function, and ψ_{nk} is a Bloch wave function with eigenvalue E_n [58]. Here, the summation is over all occupied bands. The calculated Berry curvatures of $\text{CrI}_3/\text{MoSi}_2\text{P}_4$ and $\text{CrI}_3/\text{WSi}_2\text{P}_4$ heterostructures are shown in Figs. 5(a) and 5(b). It can be seen that the absolute values of the Berry curvatures of the two heterostructures are equal but opposite in magnitude in the K and K' valleys. Therefore, hole doping can be used to induce the valley Hall effect in experiments. Especially, the $\text{CrI}_3/\text{WSi}_2\text{P}_4$ heterostructure, due to its large spin splitting and the fact that the VBM and CBM are located in the K and K' valleys, is a promising candidate for achieving spin Hall effect devices [14].

The nonzero Berry curvature indicates that the Dirac valley has chirality, which can be described by the circularly polarized light selection rule. Mathematically, circular polarization

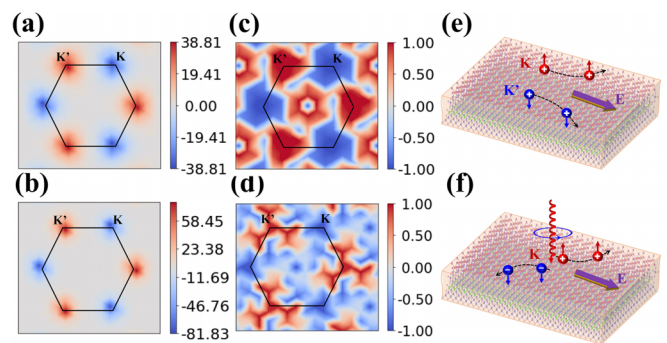


FIG. 5. (a) and (b) show the Berry curvature distributions for all valence bands of the $\text{CrI}_3/\text{MoSi}_2\text{P}_4$ and $\text{CrI}_3/\text{WSi}_2\text{P}_4$ heterostructures, respectively. (c) and (d) show the circular polarization η calculated for the $\text{CrI}_3/\text{MoSi}_2\text{P}_4$ and $\text{CrI}_3/\text{WSi}_2\text{P}_4$ heterostructures, respectively. (e) shows the spin and valley Hall effect diagram in hole-doped $\text{CrI}_3/\text{MoSi}_2\text{P}_4$ and $\text{CrI}_3/\text{WSi}_2\text{P}_4$ heterostructures. The red (blue) spheres represent carriers from the K (K') valley, and the up (down) arrows indicate spin up (spin down). (f) shows the spin and valley Hall effect diagram of the $\text{CrI}_3/\text{MoSi}_2\text{P}_4$ and $\text{CrI}_3/\text{WSi}_2\text{P}_4$ heterostructures under right circularly polarized light at a specific frequency. The + and - symbols in the spheres represent holes and electrons, respectively. The up (down) arrows indicate the up (down) spin component.

is defined as

$$\eta(\mathbf{k}) = \frac{|P_+(\mathbf{k})|^2 - |P_-(\mathbf{k})|^2}{|P_+(\mathbf{k})|^2 + |P_-(\mathbf{k})|^2}, \quad (6)$$

where $P_{\pm}(\mathbf{k}) = \langle c\mathbf{k} | p_x \pm ip_y | v\mathbf{k} \rangle$ is the interband transition matrix, which describes the vertical transitions of electrons at point k from the valence band v to the conduction band c under the radiation fields of left and right spin polarization [59]. The k -resolved circular polarization of the $\text{CrI}_3/\text{MoSi}_2\text{P}_4$ and $\text{CrI}_3/\text{WSi}_2\text{P}_4$ heterostructures is shown in Figs. 5(c) and 5(d), respectively. Owing to the protection of time reversal symmetry, the right-handed (σ^+) circular polarization photons can be selectively absorbed in the K valley, and electrons in the K valley are excited from the valence band to the conduction band. This means that the right (left) circularly polarized light is locked with the K (K') valley. Consequently, σ^- circular polarization photons can be selectively absorbed only in the K' valley. Therefore, in two unequal K and K' valleys, circularly polarized light pumping can selectively generate electrons and holes in only one desirable valley, which is similar to the situation in 2D MoS_2 [6].

Based on the above analysis, considering that Berry curvature can be equivalent to an effective magnetic field in momentum space, when a longitudinal electric field is applied, the carrier will obtain an abnormal lateral velocity v_{\perp} . The size of v_{\perp} is proportional to the cross product of $\vec{E} \times \vec{\Omega}$. Due to the opposite Berry curvatures in the K and K' valleys, electrons in the K and K' valleys will obtain opposite v_{\perp} and move in opposite directions, resulting in the valley Hall effect. In addition, due to spin valley coupling, the spin Hall effect is also expected to occur, as shown in Fig. 5(e). When the Fermi level is located between the spin states of two valleys in the valence band by hole doping, the opposite Berry curvatures of the K and K' valleys drive carriers with different spins to

gather on both sides, resulting in the accumulation of spins on the opposite boundary. In addition to hole doping, the valley Hall effect can also be achieved through optical pumping. As shown in Fig. 5(f). The optically generated carriers selectively excited by circularly polarized light will obtain the opposite transverse velocity, which is due to their opposite Berry curvature. This leads to the valley Hall effect with Hall current, which can be detected as voltage. Specifically, the additional spin Hall effect benefits from the strong spin valley coupling in the $\text{CrI}_3/\text{MSi}_2\text{P}_4$ heterostructures. The coexistence of spin and valley Hall effects will contribute to practical valleytronic applications.

Generally, in the absence of a ferromagnetic CrI_3 substrate, $\text{Mo}/\text{WSi}_2\text{P}_4$ can achieve valley polarization through circular or ultrashort pulses [20,60]. However, due to the participation of phonons, complex luminescence processes and valley to valley scattering occur during the excitation of valley polarization. Consequently, the measured valley polarization is strictly dependent on sample quality and experimental conditions [61], impeding experimental realization. Meanwhile, the dynamic valley polarization of optical transitions dominated by neutral excitons usually disappears within a few picoseconds [62]. The issues mentioned above greatly limit the practical application of valley polarization in valleytronic devices. The ferromagnetic CrI_3 substrate induces a magnetic proximity effect to break time reversal symmetry, leading to sustainable valley polarization. In addition, due to the tunability of vertical strain, valley polarization and spin splitting can be manipulated simultaneously. This suggests the creation of a degree of freedom to polarization [63]. The vertical strain can be controlled by vacuum thermal annealing or pressure at the tip of a scanning tunneling microscope or external hydrostatic pressure, and the vdW heterostructures can be stabilized by using an *h*-BN passivation layer [47,64,65]. This significantly

enhances the possibility of experimental achievement in the future.

IV. CONCLUSIONS

In general, we systematically studied the structural stability and electronic properties of $\text{CrI}_3/\text{MSi}_2\text{P}_4$ heterostructures. The results show the following: (1) K and K' valley splitting in $\text{CrI}_3/\text{MSi}_2\text{P}_4$ heterostructures is mainly caused by the time reversal symmetry breaking, and the coupling between valley spin in the valence band/conduction band and the magnetic field of the CrI_3 substrate dominates the total valley splitting. (2) The amplitude of the valley splitting is mainly influenced by the distance between Mo/W atoms and Cr atoms, and due to the outermost P and Si sublayers, the charge transfer between Mo/W and Cr atoms and the induced magnetic moment in Mo/W are significantly limited. Therefore, the valley polarization of $\text{CrI}_3/\text{MSi}_2\text{P}_4$ heterostructures is controllable and robust. (3) By using the 2D ferromagnetic CrI_3 monolayer as a substrate, moderate and tunable valley splitting of the $\text{Mo}/\text{WSi}_2\text{P}_4$ monolayer can be achieved. Our theoretical explorations have offered some understanding of the manipulation of valley degeneracy and the valley enhancement mechanism in MA_2Z_4 -based heterostructures by using ferromagnetic substrates, facilitating practical application of valleytronics in the future.

ACKNOWLEDGMENTS

This work was supported by the National Natural Science Foundation of China (Grants No. 62174088, No. 62371238, and No. 61871227). We are grateful to the High-Performance Computing Centre of Nanjing University for providing the IBM Blade cluster system.

-
- [1] D. Xiao, W. Yao, and Q. Niu, Valley-Contrasting Physics in Graphene: Magnetic Moment and Topological Transport, *Phys. Rev. Lett.* **99**, 236809 (2007).
 - [2] H. Zeng, J. Dai, W. Yao, D. Xiao, and X. Cui, Valley polarization in MoS_2 monolayers by optical pumping, *Nat. Nanotechnol.* **7**, 490 (2012).
 - [3] Y. Kim and J. D. Lee, Proposed Valley Valve from Four-Channel Valley Manipulation, *Phys. Rev. Appl.* **11**, 034048 (2019).
 - [4] K. F. Mak, C. Lee, J. Hone, J. Shan, and T. F. Heinz, Atomically Thin MoS_2 : A New Direct-Gap Semiconductor, *Phys. Rev. Lett.* **105**, 136805 (2010).
 - [5] Z. Y. Zhu, Y. C. Cheng, and U. Schwingenschloegl, Giant spin-orbit-induced spin splitting in two-dimensional transition-metal dichalcogenide semiconductors, *Phys. Rev. B* **84**, 153402 (2011).
 - [6] D. Xiao, G.-B. Liu, W. Feng, X. Xu, and W. Yao, Coupled Spin and Valley Physics in Monolayers of MoS_2 and Other Group-VI Dichalcogenides, *Phys. Rev. Lett.* **108**, 196802 (2012).
 - [7] X. Qian, J. Liu, L. Fu, and J. Li, Quantum spin Hall effect in two-dimensional transition metal dichalcogenides, *Science* **346**, 1344 (2014).
 - [8] K. F. Mak, K. L. McGill, J. Park, and P. L. McEuen, The valley Hall effect in MoS_2 transistors, *Science* **344**, 1489 (2014).
 - [9] E. S. Penev, N. Marzari, and B. I. Yakobson, Theoretical prediction of two-dimensional materials, behavior, and properties, *ACS Nano* **15**, 5959 (2021).
 - [10] Y.-L. Hong, Z. Liu, L. Wang, T. Zhou, W. Ma, C. Xu, S. Feng, L. Chen, M.-L. Chen, D.-M. Sun, X.-Q. Chen, H.-M. Cheng, and W. Ren, Chemical vapor deposition of layered two-dimensional MoSi_2N_4 materials, *Science* **369**, 670 (2020).
 - [11] J. Yu, J. Zhou, X. Wan, and Q. Li, High intrinsic lattice thermal conductivity in monolayer MoSi_2N_4 , *New J. Phys.* **23**, 033005 (2021).
 - [12] R. Chen, D. Chen, and W. Zhang, First-principles calculations to investigate stability, electronic and optical properties of fluorinated MoSi_2N_4 monolayer, *Results Phys.* **30**, 104864 (2021).
 - [13] H. Ai, D. Liu, J. Geng, S. Wang, K. H. Lo, and H. Pan, Theoretical evidence of the spin-valley coupling and valley polarization in two-dimensional MoSi_2X_4 ($X = \text{N}, \text{P}, \text{As}$), *Phys. Chem. Chem. Phys.* **23**, 3144 (2021).
 - [14] J. Yuan, Q. Wei, M. Sun, X. Yan, Y. Cai, L. Shen, and U. Schwingenschloegl, Protected valley states and generation of

- valley- and spin-polarized current in monolayer MA_2Z_4 , *Phys. Rev. B* **105**, 195151 (2022).
- [15] J. Zhao, X. Jin, H. Zeng, C. Yao, and G. Yan, Spin-valley coupling and valley splitting in the $MoSi_2N_4/CrCl_3$ van der Waals heterostructure, *Appl. Phys. Lett.* **119**, 213101 (2021).
- [16] S.-D. Guo, X.-S. Guo, G.-Z. Wang, K. Cheng, and Y.-S. Ang, Electric-field induced magnetic-anisotropy transformation to achieve spontaneous valley polarization, *J. Mater. Chem. C* **10**, 16363 (2022).
- [17] H.-X. Cheng, J. Zhou, W. Ji, Y.-N. Zhang, and Y.-P. Feng, Two-dimensional intrinsic ferrovalley GdI_2 with large valley polarization, *Phys. Rev. B* **103**, 125121 (2021).
- [18] K. Sheng, Q. Chen, H.-K. Yuan, and Z.-Y. Wang, Monolayer CeI_2 : An intrinsic room-temperature ferrovalley semiconductor, *Phys. Rev. B* **105**, 075304 (2022).
- [19] P. Jiang, L. Kang, Y.-L. Li, X. Zheng, Z. Zeng, and S. Sanvito, Prediction of the two-dimensional Janus ferrovalley material $LaBrI$, *Phys. Rev. B* **104**, 035430 (2021).
- [20] K. F. Mak, K. He, J. Shan, and T. F. Heinz, Control of valley polarization in monolayer MoS_2 by optical helicity, *Nat. Nanotechnol.* **7**, 494 (2012).
- [21] T. Smolenski, M. Goryca, M. Koperski, C. Faugeras, T. Kazimierzczuk, A. Bogucki, K. Nogajewski, P. Kossacki, and M. Potemski, Tuning Valley Polarization in a WSe_2 Monolayer with a Tiny Magnetic Field, *Phys. Rev. X* **6**, 021024 (2016).
- [22] Y. C. Cheng, Q. Y. Zhang, and U. Schwingenschloegl, Valley polarization in magnetically doped single-layer transition-metal dichalcogenides, *Phys. Rev. B* **89**, 155429 (2014).
- [23] J. J. Hauser, Magnetic proximity effect, *Phys. Rev.* **187**, 580 (1969).
- [24] A. Zhang, Z. Gong, Z. Zhu, A. Pan, and M. Chen, Effects of the substrate-surface reconstruction and orientation on the spin valley polarization in $MoTe_2/EuO$, *Phys. Rev. B* **102**, 155413 (2020).
- [25] K. L. Seyler, D. Zhong, B. Huang, X. Linpeng, N. P. Wilson, T. Taniguchi, K. Watanabe, W. Yao, D. Xiao, M. A. McGuire, K.-M. C. Fu, and X. Xu, Valley manipulation by optically tuning the magnetic proximity effect in WSe_2/CrI_3 heterostructures, *Nano Lett.* **18**, 3823 (2018).
- [26] D. Zhong, K. L. Seyler, X. Linpeng, R. Cheng, N. Sivadas, B. Huang, E. Schmidgall, T. Taniguchi, K. Watanabe, M. A. McGuire, W. Yao, D. Xiao, K.-M. C. Fu, and X. Xu, Van der Waals engineering of ferromagnetic semiconductor heterostructures for spin and valleytronics, *Sci. Adv.* **3**, e1603113 (2017).
- [27] Q. Zhang, S. A. Yang, W. Mi, Y. Cheng, and U. Schwingenschloegl, Large spin-valley polarization in monolayer $MoTe_2$ on top of $EuO(111)$, *Adv. Mater.* **28**, 7044 (2016).
- [28] W.-B. Zhang, Q. Qu, P. Zhu, and C.-H. Lam, Robust intrinsic ferromagnetism and half semiconductivity in stable two-dimensional single-layer chromium trihalides, *J. Mater. Chem. C* **3**, 12457 (2015).
- [29] J. L. Lado and J. Fernandez-Rossier, On the origin of magnetic anisotropy in two dimensional CrI_3 , *2D Mater.* **4**, 035002 (2017).
- [30] G. G. Kresse and J. J. Furthmüller, Efficient iterative schemes for *ab initio* total-energy calculations using a plane-wave basis set, *Phys. Rev. B* **54**, 11169 (1996).
- [31] G. Kresse and J. Hafner, *Ab initio* molecular dynamics for liquid metals, *Phys. Rev. B* **47**, 558(R) (1993).
- [32] S. Steiner, S. Khmelevskiy, M. Marsmann, and G. Kresse, Calculation of the magnetic anisotropy with projected-augmented-wave methodology and the case study of disordered $Fe_{1-x}Co_x$ alloys, *Phys. Rev. B* **93**, 224425 (2016).
- [33] J. P. Perdew, K. Burke, and M. Ernzerhof, Generalized Gradient Approximation Made Simple, *Phys. Rev. Lett.* **77**, 3865 (1996).
- [34] H. J. Monkhorst and J. D. Pack, Special points for Brillouin-zone integrations, *Phys. Rev. B* **13**, 5188 (1976).
- [35] See Supplemental Material at <http://link.aps.org/supplemental/10.1103/PhysRevB.108.125304> for the geometric structure parameters, projection band, Berry curvature, and circularly polarized polarization of the CrI_3 monolayer and Mo/WSi_2P_4 monolayers; the geometric parameters of the $CrI_3/MoSi_2P_4$ heterostructure for different functions; the AIMD simulation of $CrI_3/MoSi_2P_4$ heterostructures; the projection band structure of the CrI_3/WSi_2P_4 heterostructure in different magnetization directions; the charge density difference, work function, and band alignment of the CrI_3/WSi_2P_4 heterostructure; the valley splitting changes in the CrI_3/WSi_2P_4 heterostructure under different vertical compressive strains; Bader charge analysis of the CrI_3/WSi_2P_4 heterostructure; the band structure of the $CrI_3/MoSi_2P_4$ heterostructure under electric field; the magnetic moment changes in $CrI_3/MoSi_2P_4$ heterostructures under vertical compressive strain; and an estimation method for the Curie temperature of the $CrI_3/MoSi_2P_4$ heterostructure.
- [36] J. Klimeš, D. R. Bowler, and A. Michaelides, Van der Waals density functionals applied to solids, *Phys. Rev. B* **83**, 195131 (2011).
- [37] M. A. McGuire, H. Dixit, V. R. Cooper, and B. C. Sales, Coupling of crystal structure and magnetism in the layered, ferromagnetic insulator CrI_3 , *Chem. Mater.* **27**, 612 (2015).
- [38] T. Thonhauser, V. R. Cooper, S. Li, A. Puzder, P. Hyldgaard, and D. C. Langreth, Van der Waals density functional: Self-consistent potential and the nature of the van der Waals bond, *Phys. Rev. B* **76**, 125112 (2007).
- [39] K. Momma and F. Izumi, VESTA 3 for three-dimensional visualization of crystal, volumetric and morphology data, *J. Appl. Crystallogr.* **44**, 1272 (2011).
- [40] L. Webster, L. Liang, and J.-A. Yan, Distinct spin-lattice and spin-phonon interactions in monolayer magnetic CrI_3 , *Phys. Chem. Chem. Phys.* **20**, 23546 (2018).
- [41] C. Liu, Z. Wang, W. Xiong, H. Zhong, and S. Yuan, Effect of vertical strain and in-plane biaxial strain on type-II $MoSi_2N_4/Cs_3Bi_2I_9$ van der Waals heterostructure, *J. Appl. Phys.* **131**, 163102 (2022).
- [42] P. Zhao, Z.-Y. Jiang, J.-M. Zheng, Y.-M. Lin, and A. Du, Theoretical study of a novel $WSi_2N_4/MoSi_2N_4$ heterostructure with ultrafast carrier transport, *J. Phys. Chem. C* **126**, 11380 (2022).
- [43] C. Ke, Y. Wu, W. Yang, Z. Wu, C. Zhang, X. Li, and J. Kang, Large and controllable spin-valley splitting in two-dimensional WS_2/h -VN heterostructure, *Phys. Rev. B* **100**, 195435 (2019).
- [44] M. Ezawa, Valley-Polarized Metals and Quantum Anomalous Hall Effect in Silicene, *Phys. Rev. Lett.* **109**, 055502 (2012).
- [45] M. Tahir, A. Manchon, K. Sabeeh, and U. Schwingenschloegl, Quantum spin/valley Hall effect and topological insulator phase transitions in silicene, *Appl. Phys. Lett.* **102**, 162412 (2013).
- [46] Z. Zhang, X. Ni, H. Huang, L. Hu, and F. Liu, Valley splitting in the van der Waals heterostructure WSe_2/CrI_3 : The role of atom superposition, *Phys. Rev. B* **99**, 115441 (2019).

- [47] B. Fulop, A. Marffy, E. Tovari, M. Kedves, S. Zihlmann, D. Indolese, Z. Kovacs-Krausz, K. Watanabe, T. Taniguchi, C. Schoenenberger, I. Kezsmarki, P. Makk, and S. Csonka, New method of transport measurements on van der Waals heterostructures under pressure, *J. Appl. Phys.* **130**, 064303 (2021).
- [48] L. Xu, M. Yang, L. Shen, J. Zhou, T. Zhu, and Y. P. Feng, Large valley splitting in monolayer WS_2 by proximity coupling to an insulating antiferromagnetic substrate, *Phys. Rev. B* **97**, 041405(R) (2018).
- [49] R. J. Sun, J. J. Lu, X. W. Zhao, G. C. Hu, X. B. Yuan, and J. F. Ren, Robust valley polarization induced by superexchange effects in HfNX ($X=\text{Cl, Br, I}$)/ FeCl_2 two-dimensional ferrovalley heterostructures, *Appl. Phys. Lett.* **120**, 063103 (2022).
- [50] W. Tang, E. Sanville, and G. Henkelman, A grid-based Bader analysis algorithm without lattice bias, *J. Phys.: Condens. Matter* **21**, 084204 (2009).
- [51] X.-J. Dong, K. Jia, W.-X. Ji, S.-S. Li, and C.-W. Zhang, Valleytronics candidate with spontaneous valley polarization in a-type antiferromagnetic $\text{MoSi}_2\text{N}_4/\text{MnPS}_3$ heterostructure, *ACS Appl. Electron. Mater.* **5**, 2046 (2023).
- [52] Q. Wang, L. Cao, S.-J. Liang, W. Wu, G. Wang, C. H. Lee, W. L. Ong, H. Y. Yang, L. K. Ang, S. A. Yang, and Y. S. Ang, Efficient ohmic contacts and built-in atomic sublayer protection in MoSi_2N_4 and WSi_2N_4 monolayers, *npj 2D Mater Appl.* **5**, 71 (2021).
- [53] Y. S. Ang, S. A. Yang, C. Zhang, Z. Ma, and L. K. Ang, Valleytronics in merging Dirac cones: All-electric-controlled valley filter, valve, and universal reversible logic gate, *Phys. Rev. B* **96**, 245410 (2017).
- [54] S. S. Baik, K. S. Kim, Y. Yi, and H. J. Choi, Emergence of two-dimensional massless Dirac fermions, chiral pseudospins, and Berry's phase in potassium doped few-layer black phosphorus, *Nano Lett.* **15**, 7788 (2015).
- [55] J. Kim, S. S. Baik, S. H. Ryu, Y. Sohn, S. Park, B.-G. Park, J. Denlinger, Y. Yi, H. J. Choi, and K. S. Kim, Observation of tunable band gap and anisotropic Dirac semimetal state in black phosphorus, *Science* **349**, 723 (2015).
- [56] J. Kim, S. S. Baik, S. W. Jung, Y. Sohn, S. H. Ryu, H. J. Choi, B.-J. Yang, and K. S. Kim, Two-Dimensional Dirac Fermions Protected by Space-Time Inversion Symmetry in Black Phosphorus, *Phys. Rev. Lett.* **119**, 226801 (2017).
- [57] S. Teng, X. Mao, Z. Liu, Y. Liu, X. Xu, L. Li, X. Xie, S. Fan, G. Zhou, J. Li, and J. Li, Manipulation of valley splitting for the $\text{WSe}_2/\text{NiCl}_2$ heterostructure by adjusting the interlayer spacing and constructing a $\text{NiCl}_2/\text{WSe}_2/\text{NiCl}_2$ heterojunction, *New J. Phys.* **22**, 103061 (2020).
- [58] Y. G. Yao, L. Kleinman, A. H. MacDonald, J. Sinova, T. Jungwirth, D. S. Wang, E. G. Wang, and Q. Niu, First Principles Calculation of Anomalous Hall Conductivity in Ferromagnetic bcc Fe, *Phys. Rev. Lett.* **92**, 037204 (2004).
- [59] T. Cao, G. Wang, W. Han, H. Ye, C. Zhu, J. Shi, Q. Niu, P. Tan, E. Wang, B. Liu, and J. Feng, Valley-selective circular dichroism of monolayer molybdenum disulphide, *Nat. Commun.* **3**, 887 (2012).
- [60] F. Nematollahi, S. A. O. Motlagh, J.-S. Wu, R. Ghimire, V. Apalkov, and M. I. Stockman, Topological resonance in Weyl semimetals in a circularly polarized optical pulse, *Phys. Rev. B* **102**, 125413 (2020).
- [61] Y. Li, B. Yang, S. Xu, B. Huang, and W. Duan, Emergent phenomena in magnetic two-dimensional materials and van der Waals heterostructures, *ACS Appl. Electron. Mater.* **4**, 3278 (2022).
- [62] Y. Ye, J. Xiao, H. Wang, Z. Ye, H. Zhu, M. Zhao, Y. Wang, J. Zhao, X. Yin, and X. Zhang, Electrical generation and control of the valley carriers in a monolayer transition metal dichalcogenide, *Nat. Nanotechnol.* **11**, 598 (2016).
- [63] Z. Liu, Y. Han, Y. Ren, Q. Niu, and Z. Qiao, Van der Waals heterostructure $\text{Pt}_2\text{HgSe}_3/\text{CrI}_3$ for topological valleytronics, *Phys. Rev. B* **104**, L121403 (2021).
- [64] S. Tongay, W. Fan, J. Kang, J. Park, U. Koldemir, J. Suh, D. S. Narang, K. Liu, J. Ji, J. Li, R. Sinclair, and J. Wu, Tuning interlayer coupling in large-area heterostructures with CVD-Grown MoS_2 and WS_2 monolayers, *Nano Lett.* **14**, 3185 (2014).
- [65] M. Yankowitz, K. Watanabe, T. Taniguchi, P. San-Jose, and B. J. LeRoy, Pressure-induced commensurate stacking of graphene on boron nitride, *Nat. Commun.* **7**, 13168 (2016).